

Linking stability with molecular geometries of perovskites and lanthanide richness using machine learning methods

Sampreeti Bhattacharya*

and

Arkaprava Roy†

April 24, 2023

Abstract: Oxide perovskite materials of type ABO_3 have a wide range of technological applications, such as catalysts in solid oxide fuel cells and as light-absorbing materials in solar photovoltaics. These materials often exhibit differential structural and electrostatic properties through lanthanide or non-lanthanide derived A- and B- sites. Although, experimental and/or computational verification of these differences are often difficult. In this paper, we thus take a data-driven approach. Specifically, we run three analysis using the dataset Li, Jacobs, and Morgan [2018a] applying advanced machine learning tools to perform nonparametric regressions and also to produce data visualizations using latent factor analysis (LFA) and principal component analysis (PCA). We also implement a nonparametric feature screening step while performing our high dimensional regression analysis, ensuring robustness in our results.

Keywords: Geometric descriptors, Materials Information, Perovskites, Stability.

1 Introduction

Perovskites are fascinating systems due to their intriguing physicochemical features and capacity to boost a wide range of electromagnetic and thermal processes. Owing to their ferromagnetic, ferroelectric, and piezoelectric characteristics, as well as ion conductivity, photocatalysis, and superconductivity applications, perovskite systems have a wide range of application [Hayward, Cussen, Claridge, Bieringer, Rosseinsky, Kiely, Blundell, Marshall, and Pratt, 2002, Jin, Zhou, Goodenough, Liu, Zhao, Yang, Yu, Yu, Katsura, Shatskiy, et al., 2008, Yamada, Takata, Hayashi, Shinohara, Azuma, Mori, Muranaka, Shimakawa, and Takano, 2008, Belik, Glazkova, Katsuya, Tanaka, Sobolev, and Presniakov, 2016]. These materials are potently versatile in optoelectronic and spintronic applications, and their formation and stability is governed by atomistic metrics such as tolerance factor (t) and octahedral factor (μ), where $t = (r_A + r_X) / \sqrt{2}(r_B + r_X)$ and $\mu = (r_B / r_X)$ respectively [Goldschmidt, 1926]. For stable perovskite compounds, these t values are

*Department of Chemistry, University of North Carolina at Chapel Hill, Chapel Hill, NC, USA

†Department of Biostatistics, University of Florida, Gainesville, FL, USA

in the range of 0.75 to 1.05, and μ values range from 0.00 to 0.15. [Filip and Giustino, 2018, Zhao, Gao, Li, Qian, Shen, Wang, Shen, Hu, Dong, Huang, et al., 2021].

In ABO_3 type oxide perovskite systems, the 12-fold coordinated A-sites are occupied by large size alkali metal ions, alkaline earth metal ions or lanthanide cations, while the 6-fold coordinated B-sites, are occupied by transition metals [Wexler, Gautam, Stechel, and Carter, 2021]. The chemical diversity in oxide perovskites makes the class of compound extremely tunable [Gopalakrishnan, Sebastian, and Ahn, 2020, Li, Lin, Liu, Hu, Cao, Chen, and Xing, 2022], at the same time raising an issue of incorrect identification of formable systems and the associated stability [Li, Wang, Deschler, Gao, Friend, and Cheetham, 2017]. In this work, we study mixture of ABO_3 perovskite systems [Bendersky, Greenblatt, and Chen, 2003, Liang, Tang, Shao, Li, Zeng, and Zheng, 2008, Nag and Shubha, 2014], where the A^+ sites metal cations are in ternary, quaternary and sextenary types of environment attributed to the B^+ site cations, and connected individual octahedra [Zhou, 2020]. The multitude of possible combinations in these metal cations leads to varying structural dependence on thermodynamic and electronic properties. Accordingly, the two most fundamental metrics that link the stability of geometries based on the spatial arrangement of atoms in a lattice are the octahedral factor and the Goldschmidt tolerance factor.

The studies in Giaquinta and Zur Loye [1994], Goudochnikov and Bell [2007], Filip and Giustino [2018], Liang, Lin, Lan, Meng, Zhao, Zou, Castelli, Pullerits, Canton, and Zheng [2020] demonstrate the efficacy of structural predictors in predicting the stability of perovskites. According to Filip and Giustino [2018], these metrics can achieve an accuracy as high as 80% in predicting stability and formable perovskites. Albeit, these identifiers are susceptible to electrostatic interactions such as Jahn-Teller (JT) distortions [Hong, Byeon, Bak, Heo, Kim, Bae, and Chung, 2021] and thermal motions of the crystal geometry. Alongside, spatial arrangement of BO_3 octahedra and octahedral rotations are also linked with Glazer modes [Glazer and Megaw, 1972, Aleksandrov and Bartolomé, 2001]. These geometric modes are capable of tuning the global and local symmetry of the crystal, thereby making structural distortions a crucial descriptor in identifying significant electronic properties [Jia, Hu, Xu, Gao, Zhao, Barone, Stroppa, and Ren, 2020].

In recent work by Hong et al. [2021] lanthanide based inorganic perovskites show structural attributes induced by local charge separation. As explained in Hong et al. [2021] JT effect contributes to spontaneous lengthening of bonds caused by the tetragonal crystal field. Similarly, octahedral tilts and rotations of oxygen octahedra also play a crucial role in influencing the stability, formability, magnetic, dielectric, and catalytic properties [Glazer and Megaw, 1972, Woodward, 1997]. On the other hand, thermodynamic stability of perovskite systems can generally be connected to stability and formability [Armiento, Kozinsky, Hautier, Fornari, and Ceder, 2014, Jacobs, Mayeshiba, Booske, and Morgan, 2018] through energy above the convex hull (EHull) measured using the convex hull analysis [Liu, Rong, Malik, Canepa, Jain, Ceder, and Persson, 2015] and energy of formation (EForm) calculated using electronic structure theory such as Density Functional Theory (DFT). As also shown in [Li, Jacobs, and Morgan, 2018b], EForm can be reliably linked to EHull when using a threshold value of 40 meV/atom. However, limitations to theoretical prediction using DFT in identifying non-degenerate ground states for lanthanide materials make accurate electronic property calculations a challenging task [Ferbinteanu, Stroppa, Scarrozza, Humelnicu, Maftai, Frecus, and Cimpoesu, 2017]. As a result, data driven approaches are gaining

importance to perform computational investigation of predicting stable perovskite systems [Sun, Dougherty, Huang, Li, and Yan, 2020].

Data driven approaches can also be utilized in understanding relevant features/descriptors arising due to specific atomic environments in perovskites systems. Specifically, we are interested in the differential characteristics among these features, important for predicting stability across the lanthanide and non-lanthanide molecules.

In this paper, we run three data-driven analyses. First, we investigate the relationship between structural features and physicochemical properties of species occupying A-site and B-site atomic sites. We employ a nonparametric marginal screening algorithm [Xue and Liang, 2017] to first identify a subset of the most important descriptors for our analysis, and subsequently, we fit multivariate predictive models using the screened dataset. Second, we study the effects of lanthanide atoms on the stability of perovskites after segregating the descriptors into two groups. The first group consists of the systems with at least one lanthanide atom in their atomic sites, characterizing them as the lanthanide substructures, and equivalently, non-lanthanide substructures are defined as the systems without any lanthanide atoms. For this analysis, we only consider the subset of predictors that are identified in the screening process described in the first analysis.

The rest of the article is organized as follows. In the next section, we describe the dataset. Section 3 presents the description of models that are used in this paper. In Section 4, we describe our marginal feature screening algorithm followed by model fitting procedure. In Section 5 we present the results from our analysis, followed by some concluding remarks in Section 6.

2 Oxide perovskite dataset

The dataset for the analysis is sourced from Li et al. [2018a]. It contains the elemental properties of 1929 oxide perovskites and their phase stability energies, generated from DFT and convex hull analysis. All the associated property measurements in the curated dataset are performed at a temperature of 1073 K and an oxygen partial pressure of 0.2 atm [Jacobs et al., 2018]. These settings mimic the approximate working conditions of solid oxide fuel cell (SOFC) cathodes and hence are a more realistic dataset to train and test the dependence of elemental properties. The dataset is composed of perovskite systems comprising elements from a candidate set of A^+ cations: Ba, La, Y, Pr, Gd, Dy, Ho, Nd, Sm, Ca, Sr, Bi, Cd, Sn, Zn, B^+ cations such as Fe, V, Cr, Mn, Sc, Co, Ti, Mg, Ni, Zr, Ga, Hf, Nb, Ta, Re, Tc, Ir, Os, Ru, Rh, Al, Cu, Pt, Zn, and X^{2-} as O. In total, the dataset consists of 71 ternary (e.g. ABO_3), 1248 quaternary (e.g. $A_nA'_{1-n}BO_3$), 601 quinary (e.g. $A_nA'_{1-n}B_mB'_{1-m}O_3$) and 9 sextenary perovskite oxide systems. The dataset comprises the descriptors that are created using an extensive elemental property database of physical and chemical properties of elements in their atomic form compiled from the Materials Agnostic Platform for Informatics and Exploration (MAGPIE) [Ward, Agrawal, Choudhary, and Wolverton, 2016] and the web chemical elements’ database in Resources for Teaching Science to construct the matrix of features used to train our machine learning models. Further details about the data are available in Jacobs et al. [2018], Li et al. [2018a].

3 Analysis plan

Regression models provide a straightforward way to interpret relationships between one or more independent variables and an outcome variable. Here, we consider several regression models such as kernel ridge regression [Géron, 2017], artificial neural networks [McCulloch and Pitts, 1943], support vector regression (SVR) [Vapnik, 1999], and random forest [Breiman, 2001], for our proposed analyses. In the rest of this section, we discuss these candidate regression models in detail. Although they are all explained for univariate response for simplicity, it requires minor modifications to the respective objective functions in case of multivariate response, which is accommodated using `MultiOutputRegressor` module from scikit-learn package. For clarity, we first define some of the notations. We denote the response variable of i -th sample as y_i , corresponding to the p -dimensional predictor vector x_i for $i = 1, \dots, N$. In matrix notation, we denote X as the design matrix, such that i -th row of X is x_i and Y as the response vector, such that j -th element of Y is y_j . Thus, X is $N \times p$ dimensional matrix and that Y is an N -length vector.

For high dimensional regression, filtering out irrelevant descriptors is imperative before deploying any machine learning algorithm. Thus, from the available features, we screen a subset of important features. We apply a nonparametric marginal screening method which relies on marginal associations between the response and each predictor separately. The details are discussed in the later part of this section.

3.1 Kernel ridge regression

Kernel ridge regression is a non-linear regression method that uses the kernel method to help the ridge regression algorithm to better fit the data. It is more generally applicable than the linear regression. The loss function can be written as the following,

$$\min \left\{ \frac{1}{N} \sum_{i=1}^N \left(y_i - \sum_{j=1}^N \beta_j K(x_j, x_i) \right)^2 + \alpha \sum_{i=1}^N \beta_i^2 \right\}, \quad (1)$$

where, β is the coefficient and the hyperparameter α is a regularization parameter, penalizing the squared- L_2 norm ($\sum_{i=1}^N \beta_i^2$) of β . And $K(\cdot, \cdot)$ is the kernel function, which is often chosen depending on the data structure. The popular kernels are exponential kernel, Gaussian kernel, Epanechnikov kernel, etc. Kernel ridge regression is a good choice when non-linearity has to be better matched to the data or when the data set closely resembles the form of a known kernel. Here, we choose the Gaussian radial basis function, $\left[K(x_i, x) = \exp \left(-\frac{(x_i - x)^T (x_i - x)}{2\sigma_k^2} \right) \right]$ which is one of the most popular choices and enjoys several nice theoretical properties [Figueiredo, 2000].

3.2 Neural-net

Neural networks are also non-linear regression models. Here, we describe single layer neural net that are additive and act in two stages. As shown in the Equation 2, the derived features Z_m , also known as hidden units, are obtained from the original features as a linear combination of inputs,

and then the target Y is modelled as another linear combination of the hidden units as shown below.

$$Z_m = \sigma(\alpha_{0m} + \alpha_m^T x), m = 1, \dots, M \quad (2)$$

$$T = \beta_0 + \sum_{m=1}^M \beta_m Z_m, \quad (3)$$

$$f(x) = g(T) \quad (4)$$

where $Z = (Z_1, Z_2, \dots, Z_M)$. The coefficients α_{0m} , α_m are coefficients to the input variables and the coefficients associated with the hidden units are β_0 and β . In forming the neurons or hidden units, the basis function also known as the activation function ($\sigma(\cdot)$) can be a sigmoid function, Gaussian radial basis function, etc. In our above general architecture, the final output function, $g(T)$ is set to identity, i.e. $g(T) = T$ for regression problems. Additionally, setting activation function σ as an identity function (i.e. $\sigma(x) = x$), the neural network model reduces to a linear model. As a result, a neural network can be considered as a non-linear generalization of the linear model. For regression, the following squared error loss is used to estimate the associated parameters,

$$\min \sum_{i=1}^N (y_i - f(x_i))^2. \quad (5)$$

3.3 Support vector regression

Support vector regression (SVR) is a method analogous to the support vector machines (SVM), which is one of the most popular models for classification problems. An SVM model with linear kernel finds linear boundaries in a sizable, transformed version of the feature space and then use those boundaries to create non-linear hyperplanes under given constraints as described in Vapnik [1998], Hastie, Tibshirani, Friedman, and Friedman [2009]. SVR however runs a similar optimization for regression problems. Furthermore, instead of minimizing the squared error loss as commonly done in the most regression problems, SVR shrinks the coefficients under some constraints on the data, given as follows,

$$\min \frac{1}{2} \sum_{i=1}^p \beta_i^2, \quad (6)$$

$$\text{such that } |y_i - \beta_0 - \beta^T x_i| \leq \varepsilon, \quad (7)$$

where β is the coefficient associated with the predictors and intercept β_0 . In SVR, the level of error ε can be pre-specified to locate the best line (or hyperplane, in higher dimensions) fitting the data. Hence, the absolute error $|y_i - \beta_0 - \beta^T x_i|$ for each i is set as less than or equal to the pre-specified maximum error ε .

Running the above optimization, we are able to obtain a linear boundary given by $f(x) = \beta_0 + \beta^T x$. In non-linear SVR, we set $f(x) = \alpha_0 + \sum_{i=1}^n \alpha_i K(x_i, x)$, where $K(\cdot, \cdot)$ stands for kernel basis function. Popular choices are polynomial $[K(x_i, x) = (x_i^T x)^d]$ and Gaussian radial basis

function which is defined in Section 3.1. We train our model for both of these two choices. Non-linear SVR renders flexibility in model fitting. For optimization, the Scikit-learn implementation employs the dual problem of the aforementioned loss.

3.4 Random forest

One of the most powerful ways to model the non-linear relationships between an outcome and a set of predictors is random forest-based supervised learning. It uses an ensemble learning method for regression, making more accurate forecasts than a single model by aggregating predictions from several decision trees. For training and testing vectors x_i and y_i respectively, a decision tree splits the feature space iteratively such that samples with identical labels or target values are grouped together. A data split with m number of nodes can be represented using sub samples Q_m with N_m samples. Each of the splits consists of a feature and threshold t_m . The efficiency of the candidate split of each node is then evaluated using a loss function for regression in this paper, followed by minimization of the hyperparameters. The scheme is solved recursively for numerous subsets until the maximum depth is attained. The location of splits after first iterations are determined using some metric such as the mean squared error or Gini index Farris [2010].

3.5 Marginal feature screening

We apply a nonparametric screening method, proposed in Xue and Liang [2017] as a pre-processing step before running our analyses with high dimensional structural features as predictors. It relies on the property that a zero correlation between the response and a given feature would mean their independence when the (response, feature) pair follow a bivariate normal distribution. Hence, the joint covariance matrix of the pair will be diagonal if they are independent and jointly normal. Here, joint normality is important, as marginal normality does not necessarily lead to joint normality. The screening step thus tests bivariate normality with diagonal covariance between the response and each feature. The protocol in Xue and Liang [2017] recommends first transforming the response and each predictor into normally distributed random variables by applying non-paranormal transformations [Liu, Lafferty, and Wasserman, 2009]. Subsequently, the Henze-Zirkler (HZ) test [Henze and Zirkler, 1990] statistic is computed to statistically quantify the separation or dissimilarity between the bivariate empirical distribution and a bivariate normal distribution with diagonal covariance for each pair of (transformed response, one transformed predictor) separately. A larger value of the HZ test statistic would thus indicate a stronger association between the response and the given predictor, as then their joint distribution does not follow a bivariate normal with diagonal covariance. Hence, the predictors with large HZ test statistic values are included in the model. The necessary theoretical justifications of this procedure are provided in Xue and Liang [2017]. In this paper, we propose a minor modification to the original algorithm for our purpose to handle multivariate responses. Our modified set of steps are in Algorithm 1 and Figure 1.

4 Oxide perovskite dataset analysis

Before proceeding with our analysis, we apply min-max normalization for each feature vector. For high dimensional regressions, we apply the screening method to select top 100 features, that are

strongly related to the response. These 100 features are then used for different regression analyses. The steps are illustrated in Algorithm 1 and Figure 1 to screen M -many most relevant predictors for q -dimensional response and p -dimensional predictor.

Table 1: The optimized parameter and hyperparameter list for each model used in univariate and multivariate multiple regressions and are optimized to get the best result.

Models	Parameters/Hyperparameters for cross validation	Constant Parameters/Hyperparameters
Support Vector Regression	gamma, C	kernel=rbf
Kernel Ridge Regression	alpha, kernel, gamma	-
Neural Network	hidden_layer_sizes,	activation=logistic, solver=lbfgs, alpha=0.001, learning_rate=constant
Random Forest	n_estimators, max_samples	criterion=squared_error

Algorithm 1: Marginal screening workflow

- (i) Input: $\mathbf{y}^1, \dots, \mathbf{y}^q$ are q response variables; $\mathbf{x}^1, \dots, \mathbf{x}^p$ are vectors of p predictors;
 - (ii) Compute the nonparanormal transformations [Liu et al., 2009] $\tilde{\mathbf{y}}^j = \Phi^{-1}(F_{\mathbf{y}^j}^j(\mathbf{y}^j))$ for $j = 1, \dots, q$. Similarly, evaluate $\tilde{\mathbf{x}}^k = \Phi^{-1}(F_{\mathbf{x}^k}^k(\mathbf{x}^k))$ for $k = 1, \dots, p$.
($\Phi(\cdot)$ = Cumulative distribution function of univariate normal and $F_{\mathbf{y}^j}^j(\cdot)$ = Cumulative distribution function of \mathbf{y}^j)
 - (iii) For each pair $(\tilde{\mathbf{y}}^j, \tilde{\mathbf{x}}^k)$, compute HZ test statistic $a_{j,k}$ which is used to test the hypothesis $H_0 : (\tilde{\mathbf{y}}^j, \tilde{\mathbf{x}}^k) \sim \text{Normal}(0, I_2)$ (Larger value implies greater dependence)
 - (iv) For each predictor, get $b_k = \sum_j a_{j,k}$
 - (v) Pick the top M predictors with the highest b_k -values.
-

In our perovskite data application, we have $q = 7$, $p = 955$ and set $M = 100$. We can summarize our analyses primarily in three parts. First, we apply a linear factor model to the screened features obtained by applying the screening steps. Factor model helps to uncover the underlying dependencies among them applying `sklearn.decomposition.FactorAnalysis` class. Here, we are primarily interested to identify the similarities and dissimilarities in their dependency structures across the lanthanide and non-lanthanide rich perovskites. Secondly, we identify the screened features, that are most relevant in explaining the seven geometric blueprints, which are 1) octahedral factor: ‘octahedral_factor’, 2) ionic octahedral factor: ‘octahedral_factor_ionic’, 3) Goldschmidt tolerance factor: ‘goldschmidt_TF_factor’, 4) ionic Goldschmidt tolerance factor : ‘goldschmidt_TF_factor_ionic’, 5) distance between cations A and oxygen atoms : ‘A_O’, 6) distance between B and oxygen atoms : ‘B_O’, and 7) the average distance between cations A and B: ‘A_B’. Finally, we investigate the varying relationship of these seven geometric features with thermodynamic stability, as measured by EHull and EForm [Li et al., 2018b] across the lanthanide and non-lanthanide substructures.

As mentioned in the previous section, we use multivariate multiple regression for our first analysis. To identify the best model, we run a predictive study using the regression models described in Section 3. We also fit linear regression models with penalties such as lasso, elastic net and ridge. However, those results are omitted owing to their extremely poor performance in com-

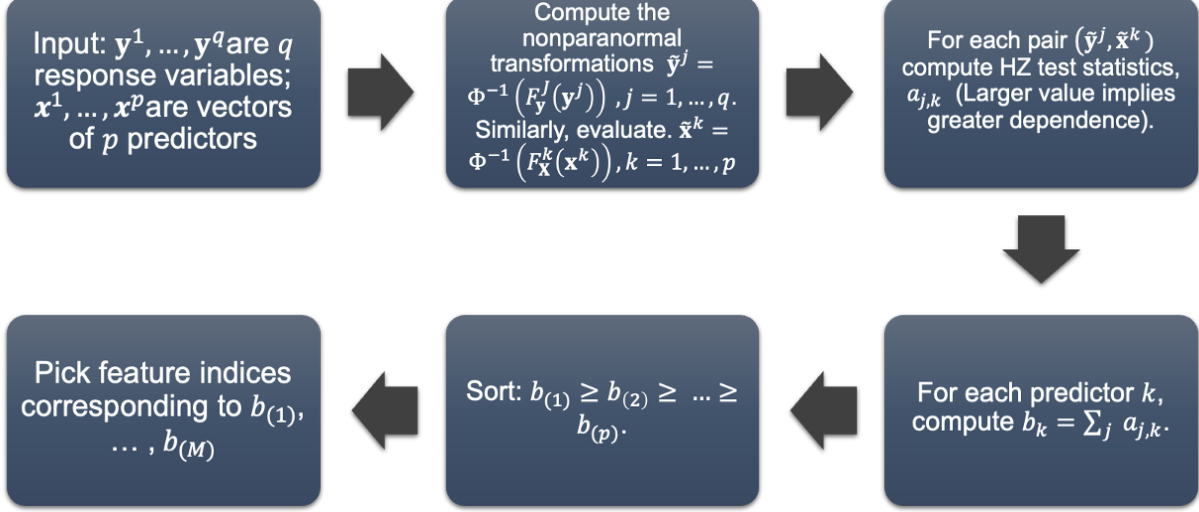


Figure 1: The workflow of the marginal screening method to select M number of features out of p predictors based on q responses, as described in Algorithm 1. In step 2, $\Phi(\cdot)$ = Cumulative distribution function of univariate normal and $F_y^j(\cdot)$ = Cumulative distribution function of y^j .

parison to the other non-linear methods. For multivariate multiple non-linear regression, we use `multioutput.MultiOutputRegressor`, which fits one regressor per target under `scikit-learn` package [Pedregosa, Varoquaux, Gramfort, Michel, Thirion, Grisel, Blondel, Prettenhofer, Weiss, Dubourg, Vanderplas, Passos, Cournapeau, Brucher, Perrot, and Duchesnay, 2011]. This is a simple and effective method for augmenting regressors that don't support multi-target regression [Pedregosa et al., 2011].

To compare across all the non-linear regression models mentioned in Table 1 we consider the out of sample Mean Squared Error (MSE). Out of sample MSE is one of the most popular metrics for model comparison as it provides a model-independent assessment of the fit, while facilitating efficient cross-method comparison. To compute the MSE, we consider 20 random test-train splits of the data. For each split, the training set consists of 80% of the data and the remaining 20 % is used to form the test set. We train each model described in Section 3 for every test-train split. In each split, the training set is used to estimate the model parameters for each model, enlisted in the second column of Table 1 applying 5-fold cross validation technique [Refaeilzadeh, Tang, Liu, et al., 2009]. Subsequently, we predict the responses utilizing the test data set for each model and compute the out of sample MSE. MSEs are further averaged over all the 20 splits to obtain a single average, described as pooled MSE estimate. The lowest pooled MSE is used to identify the candidate model, most suitable for the data. The selected model is then reapplied to the complete data to quantify the importance of each feature. Specifically, we apply the permutation importance method as implemented in `scikit-learn`. The workflow of the entire analysis is elucidated below in Figure 2

For our second analysis, we study the effect of the lanthanide atomic sites on stability and

formability of perovskites by constructing a binary group vector setting ‘1’ for perovskite with at least one lanthanide atomic site and ‘0’ otherwise. The binary group vector helps in identifying the differential characteristics across lanthanide and non lanthanide sub-structures. It is partially motivated due to the following preliminary analysis.

As an exploratory analysis, we run the principal component analysis with the combined set of seven geometric features along and EHull, EForm energy profiles and examine their differences across the two sub-structures. We show the principal components in Figures 3(a) and 3(b) where lanthanide rich sub structure illustrated using the green dots are more clustered in comparison to the non-lanthanides derived features, illustrated using the pink dots, which on the other hand are seen to be more dispersed across the PCs. These PCs explain 99 % variation of the data.

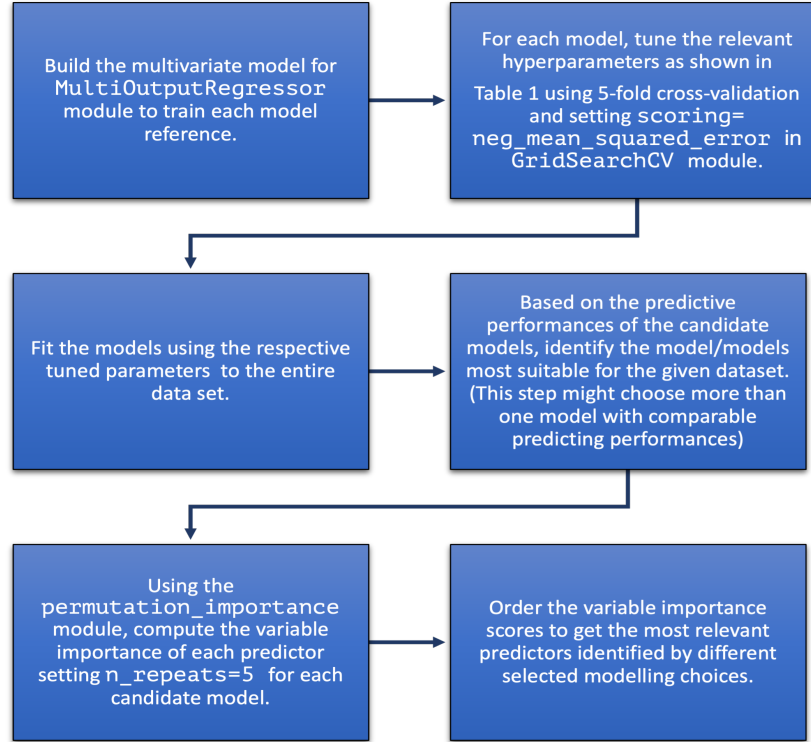


Figure 2: The workflow of the data analysis performed in this work. Based on the dimension of the response vector, the first box is used. For example, in case of 1D responses, the `MultiOutputRegressor` is not used. In the second box `GridSearchCV` is performed for different set of parameters that are used based on the model type as mentioned in Table 1. The rest of the steps are common irrespective of the model type, for `permutation_importance` the default scoring is used.

5 Results and discussion

Our overall analysis has three key parts, which are discussed in the following three subsections in detail.

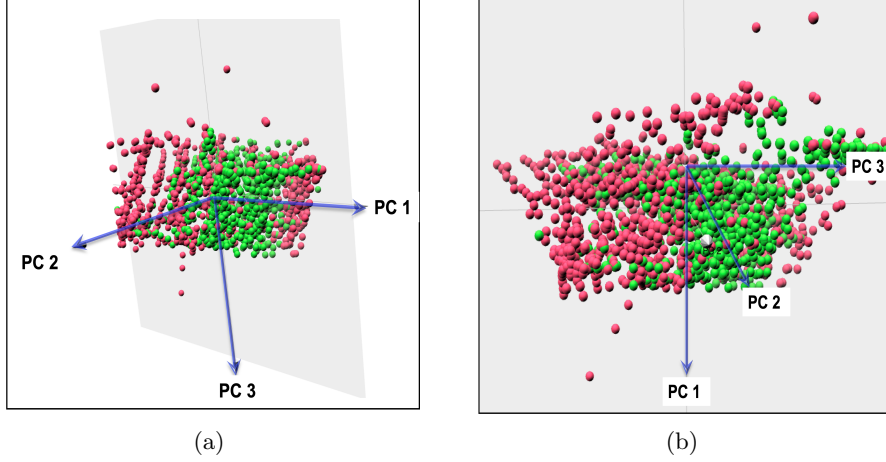


Figure 3: Principal components (PCs) are (a) shown along PC1 and (b) shown along PC2. The pink color indicate non-lanthanide substructure and the green color exhibits lanthanide substructure. Principal components are calculated using combined data, appending EHull and EForm profiles along with the seven geometric descriptors.

5.1 Differential association of screened features on the lanthanide atomic site

Geometric blueprints serve as significant features in explaining stability and formability of perovskites. Our screening procedure helps to identify top 100 elemental descriptors that are strongly associated with the blueprints. Since, the stability profile varies through doping or substitutions at A- sites or B-sites [Li, Wang, He, Liu, Long, Han, and Pan, 2015, Wang, He, Li, Liu, Long, Han, and Pan, 2016, Schader, Rossetti Jr, Luo, and Webber, 2017, Song, Li, Guo, Xu, and Fan, 2018], we analyze the differential associativity among the selected descriptors across the two sub structures.

For this analysis, we resort to the linear factor modeling, which is a natural choice for relating the multivariate data to lower-dimensional characteristics while reducing the number of parameters needed to represent the covariance. The general formula for factor analysis used is $X = F \times \lambda + \epsilon$, where X is the matrix of screened descriptors, F is a matrix of factors, λ is a matrix of factor loading and ϵ is a matrix of residuals. This method aims at getting a low-dimensional dependency pattern of the covariance [Bunte, Leppäaho, Saarinen, and Kaski, 2016]. We use `sklearn.decomposition.FactorAnalysis` class setting `n.component = 10`. Figure 4 exhibit the correlation and the estimated factors of the screened features for the lanthanide and non-lanthanide atomic sites respectively. Although, the correlation matrices in Figures 4(a) and 4(b) are relatively

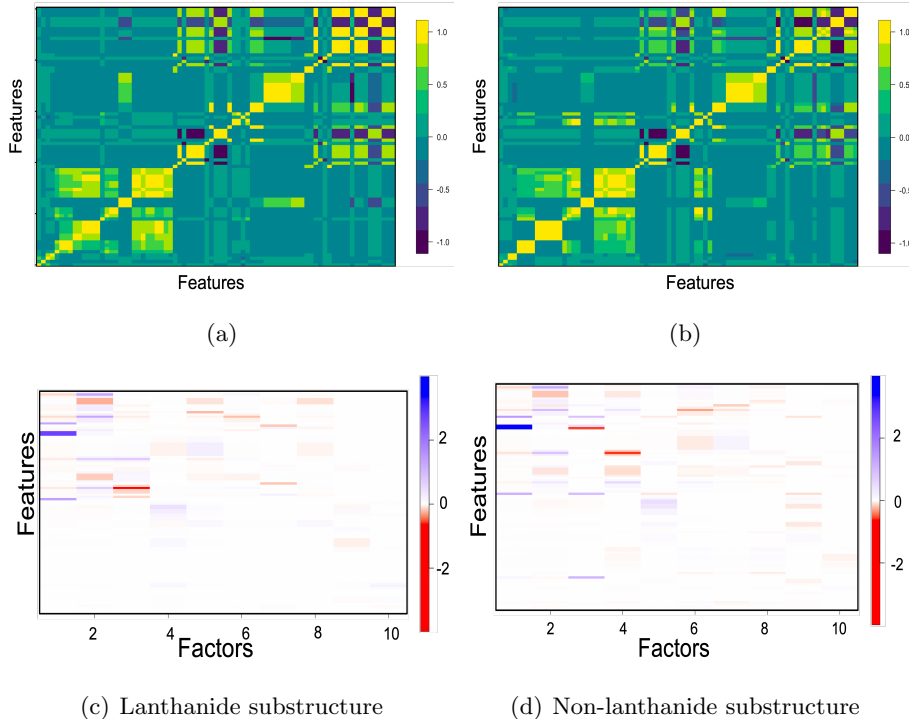


Figure 4: Correlation matrices for the 100 screened features for (a) lanthanide and (b) non-lanthanide substructures. Corresponding linear factors matrices for (c) lanthanide and (d) non lanthanide data fragments show the 10 estimated factors in the horizontal axes. For clarity the names of the variables are not reported in the figures.

similar with some differences that are identified in the factor loading (λ) matrices shown in Figures 4(c) and 4(d), indicating some differential dependency patterns after the second factor. The following subsection presents our regression analysis using these screened features.

5.2 Model assessment and relevant feature analysis

We now analyze the relationship between the seven geometric blueprints and the selected set of screened variables by applying different machine learning methods. The best model will subsequently be identified following the protocol outlined in Figure 2. As shown in Table 2 the pooled mean for out-of-sample MSEs are the lowest for random forest and kernel ridge. Numerically, it is the random forest. However, the performance of kernel ridge is almost equivalent. To obtain the most relevant features, we calculate the permutation importance setting `n_repeats=50` in `permutation_importance` from `sklearn`. We find that “Asite_shannon_radii_weighted_avg”, “Bsite_shannon_radii_weighted_avg”, “Bsite_Ionic.Radius_angstroms_weighted_avg” “shannon_radii_AB_avg” are the four most relevant features, selected by the both random forest and kernel ridge unanimously, which also suggests robustness in our inference plan of Figure 2. The conclusion corroborates with

the work by Johnsson and Lemmens [2007], where geometric features are governed primarily by the coordination number and site symmetry of the atomic positions.

Previously reported studies in [Richter, Holtappels, Graule, Nakamura, and Gauckler, 2009, Atfield, 2002] highlight that while many attributes of the perovskite systems result from the B cations, it is the A-site cations that are greatly responsible for tuning chemical and/or electronic properties. The radius of the A-site cation is essential in controlling perovskite properties, and in fact “Asite_shannon_radii_weighted_avg” is the most significant feature selected in this study. Similarly, the selection of “Bsite_Ionic.Radius_angstroms_weighted_avg” and “Bsite_shannon_radii_weighted_avg” features the B-site ionic radius and is consistent with the results reported in [Hilpert, Steinbrech, Boroomand, Wessel, Meschke, Zuev, Teller, Nickel, and Singheiser, 2003]. Such dependency emphasizes that, the expansion observed with the absence or presence of lanthanide systems is mainly determined by the relative change of the average B-site ionic radius. Although, with a decrease of the average radius of the A site ion, the BO_6 octahedra starts to tilt along a particular Glazer mode, and reduces the excess space around the A-site cation [Cherif, Dhahri, Dhahri, Oumezzine, and Vincent, 2002]. Constriction of space results in a B-O-B bond angles less than 180° while affecting the stability of the lattice. Owing to larger deviations in the A-site and B-site Shannon radii respectively, the effect of “shannon_radii_AB_avg” is also one of the significant descriptors affecting the geometric blueprints.

Table 2: Average out-of-sample MSEs over 20 random test-train splits of the data for the candidate regression models associated after regressing multivariate geometric blueprints on the fundamental elemental and non-elemental generated features in the dataset (the best performers are in bold).

Methods	Pooled Mean MSE
SVM	0.00279
Kernel Ridge	0.00046
Neural Network	0.00066
Random Forest	0.00044

5.3 Impact of geometric blueprints on EHull and EForm

We have observed the difference in the estimated latent factors associated with lanthanide and non-lanthanide substructures in Figures 4(c) and 4(d). Here we further show univariate empirical densities of the geometric blueprints for the above-mentioned substructures in Figure 5 and find that there are notable differences in the empirical densities of Goldschmidt tolerance factor and its ionic counterpart. Likewise, the densities given by the average distance between A-site and oxygen anion (‘A_O’) and A-site and B-site cation (‘A_B’) are significantly different, while densities associated with octahedral factors and the distance between the B-site and the oxygen anion (‘B_O’)

remain constant across lanthanide and non-lanthanide data-fragments. In these figures, we also report the p-values associated with nonparametric two sample Wilcoxon tests [Conover, 1999] to compare the respective lanthanide and non-lanthanide based data. A p-value smaller than 0.05 is typically considered, inferring the two groups to be statistically significantly different. Following this convention, we find that except for ‘octahedral_factor’, ‘octahedral_factor_ionic’ and ‘B_O’, the rest have significant p-values, again highlighting the above-mentioned differences.

In Table 3 we report the pooled mean of the out-of-sample MSEs, obtained by regressing geometric descriptors on EHull and EForm respectively. Pooled Mean is calculated following the working protocol mentioned in Figure 2. In this analysis, we apply SVM using `sklearn.svm.SVR`, kernel ridge using `sklearn.kernel_ridge`, Neural Network applying `sklearn.neural_network` and random forest using `sklearn.ensemble.RandomForestRegressor` from `sklearn` package. The hyperparameter optimization is done using the same protocol mentioned in Section 3. Out of the four reported errors, random forest registers the best fit for both of the two cases, with EHull and EForm as responses.

Following the protocol in Figure 2, we identify the relevant features by applying `permutation_importance` with random forest as the regression model. Importance scores may not be directly comparable in absolute scale. We thus analyze the importance score-based relative ordering of the predictors within a given analysis. As shown in Figures 6(a) and 6(b), the relative orderings of the importance values vary across the lanthanide and non-lanthanides as well as the choice of responses EHull and EForm. In Figure 6(a), all the predictors seem to have relatively equal importances in explaining EHull for non-lanthanides, but for EForm, ‘A_O’ shows a much larger effect than all the other. However, this is reversed in Figure 6(b) where ‘A_O’ shows a much larger effect for the non-lanthanides. This is an interesting finding. However, further research is needed and possibly other datasets for a confirmatory understanding. Nonetheless, ‘A_O’ is found to be the most important feature for all the cases except for lanthanides with EForm as the response.

For a comprehensive study, we subsequently repeat our above analysis adding the lanthanide indicator vector as another predictor, and show the results in Figures 6(c) and 6(d). Although the indicator vector does not appear to be the most important, it still turns out to be the second most important for EHull and also leads to a somewhat different order of importance of other predictors than the Figures 6(a) and 6(b). The distance between the A site and oxygen (‘A_O’) is found to be the most significant factor impacting EForm and EHull profiles. However, the importance of ‘B_O’, ‘octahedral_factor’ and ‘octahedral_factor_ionic’ are almost equal for both of the two cases.

6 Conclusion

Our machine learning analysis sheds light on the key structural features that govern ABO_3 type oxide perovskites, as well as the extent of correlation with the stability and formability of these compounds. Since, the regression is done using geometric blueprints as the response, it is reasonable to identify the descriptors explaining the coordination environment as the prominent features. And for the latter part, the segregation of the perovskites on the basis of lanthanides and non-lanthanides changes the trend of the geometric feature vector, thereby providing a qualitative understanding of local structural effects such as bond elongation and octahedral rotation arising due to mixed

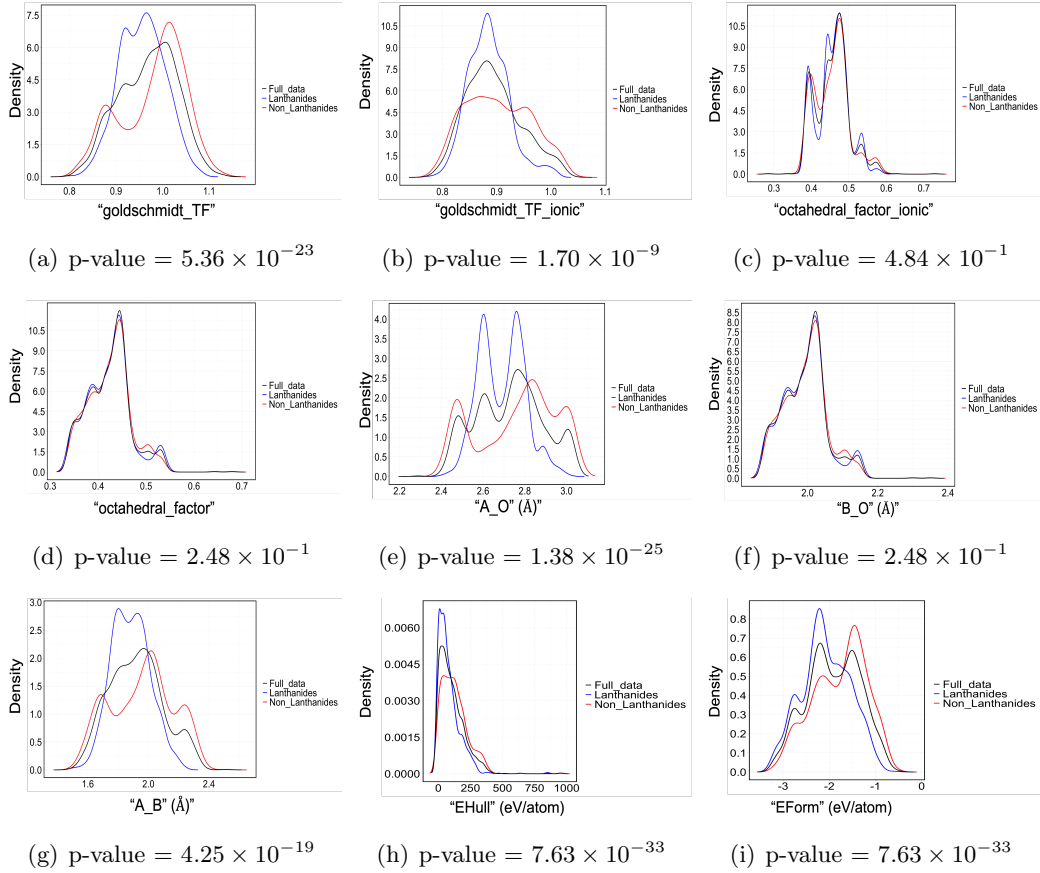


Figure 5: Empirical probability density functions for lanthanide based structures (shown in blue), non-lanthanide structures (shown in red) and the entire data (shown in black) for (a) Goldschmidt tolerance factor, (b) Goldschmidt tolerance factor with ionic radii, (c) octahedral factor with ionic radii, (d) octahedral factor, (e) distance between A and oxide ions, (f) distance between B and oxide ions and (g) the average distance between A and B cations, respectively reported in Å units. (h) EHull (i) EForm. For each case, we also compare lanthanide and non-lanthanide based data using nonparametric two-sample Wilcoxon tests and report the p-values (smaller p-value represents larger difference).

Table 3: Average out-of-sample MSEs over 20 randomiz test-train splits of the data for the candidate regression models associated after regressing EHull and EForm energy values on the seven geometric blueprints (the best performers are in bold).

Methods	Pooled Mean MSE (EHull)	Pooled Mean MSE (EForm)
SVM	0.8782	0.4620
Kernel Ridge	0.6387	0.3935
Neural Network	0.7656	0.4432
Random Forest	0.2106	0.4995

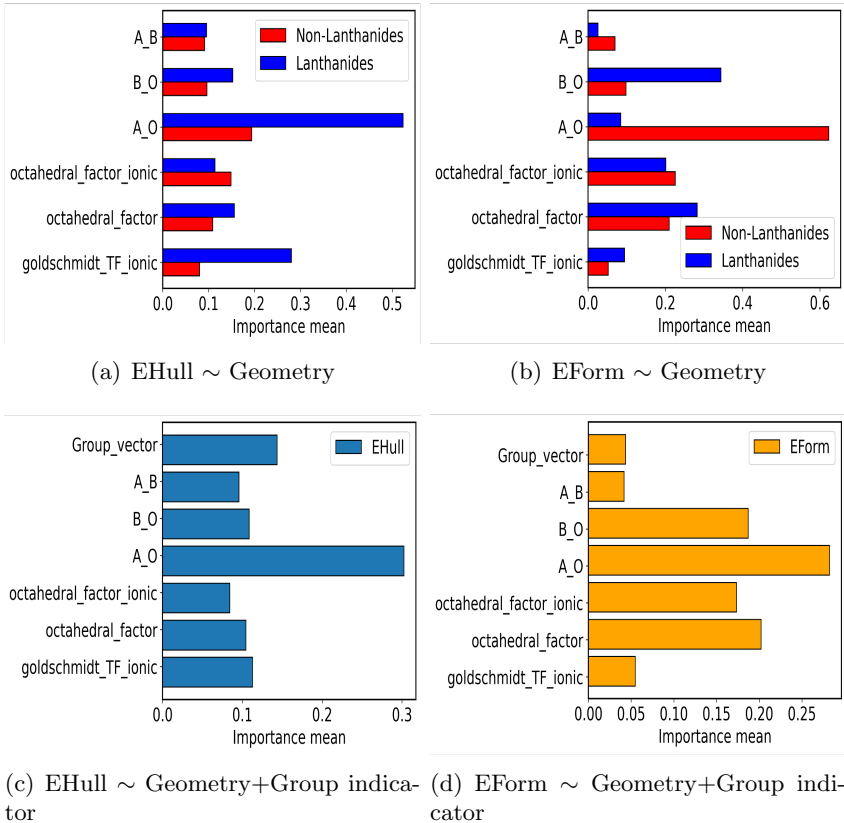


Figure 6: Bar plots showing the important features for lanthanide and non lanthanide compounds, regressing with (a) EHull as the response vector. (b) EForm as the response vector. X-axis show the selected features based on their importance mean on the Y-axis. (c)-(d) Variable importance bar plot including the binary indicator vector for EHull and EForm respectively. The abbreviation description as, TF: Tolerance Factor, A.O and B.O: average distance between A/B cation and oxygen. A.B: Average distance between A and B cations.

lanthanide atoms in the structure. For our regression-based analyses, we applied different packages from `scikit-learn`. As in any high-dimensional data-driven analysis, we too apply a screening algorithm to first select a subset of the most relevant predictors. Since the candidate regression models are mostly non-parametric, we consider a newly developed non-parametric screening method that also enjoys strong theoretical sure-screening properties [Xue and Liang, 2017]. The screened features also show differences in their latent dependency patterns. In our third analysis, we identified several differential impacts of lanthanide-richness on the EHull and EForm energy profiles.

It is true that geometric blueprints (t, μ) often fail to capture the static and dynamic rotation of octahedra associated with perovskite crystal structure [Jia, He, Akhtar, Herranz, and Pruneda, 2022]. As a result, using bond lengths and capturing any defects at A-site and B-site atoms from Scanning Electron Microscope (SEM) images [Choudhary, DeCost, Chen, Jain, Tavazza, Cohn, Park, Choudhary, Agrawal, Billinge, et al., 2022] to depict octahedral environment with related oxygen vacancies is a more quantitative approach. SEM or experimental X-Ray Diffraction data (XRD) data would certainly enrich the dataset and aid in quantifying electrostatic effects [Hong et al., 2021] through a data driven approach, which we aim to address in our future work. Also, the utility of any data-driven method relies on the quality of the data. Our current work could further be improved by utilizing electronic properties calculated with post-Hartree Fock methods [Suslick, 2001], which theoretically yield results commensurate with experimental values.

Finally, our analysis in this paper leads to several interesting findings, motivating us to run some more follow-up analyses, which will be addressed in our future works. Firstly, we can run a mediation analysis [Alwin and Hauser, 1975, MacKinnon, 2012] where the geometric features will be considered as potential mediators influencing the energy profiles after adjusting for the high dimensional structural descriptors. Secondly, it will also be interesting to study differential characteristics in the high dimensional structural blue-prints using high dimensional clustering methods across the lanthanide and non-lanthanide substructures. To address these research directions, other datasets from [Jain, Ong, Hautier, Chen, Richards, Dacek, Cholia, Gunter, Skinner, Ceder, et al., 2013, Curtarolo, Setyawan, Hart, Jahnatek, Chepulskii, Taylor, Wang, Xue, Yang, Levy, et al., 2012, Saal, Kirklin, Aykol, Meredig, and Wolverton, 2013] will also be considered.

Acknowledgement

The first author would like to thank Prof. Yosuke Kanai for his encouragement and valuable comments on this work.

Declaration of Competing Interest

The authors declare that they have no known competing financial interests or personal relationships that could have appeared to influence the work reported in this paper

Data Availability

The data is publicly available in Li et al. [2018a]. The associated codes and some additionally processed data are uploaded in <https://github.com/spriti523/Lanthanide-richness-vs-stability>. A Readme.docx file is also supplied with detailed implementation instructions and descriptions of the attached files to reproduce the results presented in this paper.

References

- KS Aleksandrov and J Bartolomé. Structural distortions in families of perovskite-like crystals. *Phase Transitions: A Multinational Journal*, 74(3):255–335, 2001.
- Duane F Alwin and Robert M Hauser. The decomposition of effects in path analysis. *American sociological review*, pages 37–47, 1975.
- Rickard Armiento, Boris Kozinsky, Geoffroy Hautier, Marco Fornari, and Gerbrand Ceder. High-throughput screening of perovskite alloys for piezoelectric performance and thermodynamic stability. *Physical Review B*, 89(13):134103, 2014.
- JP Attfield. ‘a’cation control of perovskite properties. *Crystal engineering*, 5(3-4):427–438, 2002.
- Alexei A Belik, Yana S Glazkova, Yoshio Katsuya, Masahiko Tanaka, Alexey V Sobolev, and Igor A Presniakov. Low-temperature structural modulations in CdMn7O12, CaMn7O12, SrMn7O12, and PbMn7O12 perovskites studied by synchrotron x-ray powder diffraction and mossbauer spectroscopy. *The Journal of Physical Chemistry C*, 120(15):8278–8288, 2016.
- Leonid A Bendersky, Martha Greenblatt, and Rongji Chen. Transmission electron microscopy study of ruddlesden–popper $\text{Ca}_{n+1}\text{Mn}_n\text{O}_{3n+1}$ $n=2$ and 3 compounds. *Journal of Solid State Chemistry*, 174(2):418–423, 2003.
- Leo Breiman. Random forests. *Machine learning*, 45:5–32, 2001.
- Kerstin Bunte, Eemeli Leppäaho, Inka Saarinen, and Samuel Kaski. Sparse group factor analysis for biclustering of multiple data sources. *Bioinformatics*, 32(16):2457–2463, 2016.
- K Cherif, J Dhahri, E Dhahri, M Oumezzine, and H Vincent. Effect of the a cation size on the structural, magnetic, and electrical properties of perovskites ($\text{La}_{1-x}\text{Nd}_x$) $0.7 \text{ Sr}_{0.3}\text{MnO}_3$. *Journal of Solid State Chemistry*, 163(2):466–471, 2002.
- Kamal Choudhary, Brian DeCost, Chi Chen, Anubhav Jain, Francesca Tavazza, Ryan Cohn, Cheol Woo Park, Alok Choudhary, Ankit Agrawal, Simon JL Billinge, et al. Recent advances and applications of deep learning methods in materials science. *npj Computational Materials*, 8(1):59, 2022.
- William Jay Conover. *Practical nonparametric statistics*, volume 350. john wiley & sons, 1999.

- Stefano Curtarolo, Wahyu Setyawan, Gus LW Hart, Michal Jahnatek, Roman V Chepulskii, Richard H Taylor, Shidong Wang, Junkai Xue, Kesong Yang, Ohad Levy, et al. Aflow: An automatic framework for high-throughput materials discovery. *Computational Materials Science*, 58: 218–226, 2012.
- Frank A Farris. The gini index and measures of inequality. *The American Mathematical Monthly*, 117(10):851–864, 2010.
- Marilena Ferbinteanu, Alessandro Stroppa, Marco Scarrozza, Ionel Humelnicu, Dan Maftai, Bogdan Frecus, and Fanica Cimpoesu. On the density functional theory treatment of lanthanide coordination compounds: a comparative study in a series of cu–ln (ln= gd, tb, lu) binuclear complexes. *Inorganic Chemistry*, 56(16):9474–9485, 2017.
- Mario AT Figueiredo. On gaussian radial basis function approximations: Interpretation, extensions, and learning strategies. In *Proceedings 15th International Conference on Pattern Recognition. ICPR-2000*, volume 2, pages 618–621. IEEE, 2000.
- Marina R Filip and Feliciano Giustino. The geometric blueprint of perovskites. *Proceedings of the National Academy of Sciences*, 115(21):5397–5402, 2018.
- Aurélien Géron. Hands-on machine learning with scikit-learn and tensorflow: Concepts. *Tools, and Techniques to build intelligent systems*, 2017.
- Daniel M Giaquinta and Hans-Conrad Zur Loye. Structural predictions in the abo₃ phase diagram. *Chemistry of materials*, 6(4):365–372, 1994.
- AM Glazer and Helen D Megaw. The structure of sodium niobate (t₂) at 600° c, and the cubic-tetragonal transition in relation to soft-phonon modes. *Philosophical Magazine*, 25(5):1119–1135, 1972.
- Victor Moritz Goldschmidt. Die gesetze der krystallochemie. *Naturwissenschaften*, 14(21):477–485, 1926.
- Pratheek Gopalakrishnan, Ann Rose Sebastian, and Ethan C Ahn. Perovskite oxides tunable by electromechanical and electrothermal couplings. *ECS Transactions*, 98(3):87, 2020.
- Pavel Goudochnikov and Andrew J Bell. Correlations between transition temperature, tolerance factor and cohesive energy in 2+: 4+ perovskites. *Journal of Physics: Condensed Matter*, 19(17):176201, 2007.
- Trevor Hastie, Robert Tibshirani, Jerome H Friedman, and Jerome H Friedman. *The elements of statistical learning: data mining, inference, and prediction*, volume 2. Springer, 2009.
- MA Hayward, EJ Cussen, JB Claridge, M Bieringer, MJ Rosseinsky, CJ Kiely, SJ Blundell, IM Marshall, and FL Pratt. The hydride anion in an extended transition metal oxide array: LaSrCoO₃H_{0.7}. *Science*, 295(5561):1882–1884, 2002.

- Norbert Henze and B Zirkler. A class of invariant consistent tests for multivariate normality. *Communications in statistics-Theory and Methods*, 19(10):3595–3617, 1990.
- K Hilpert, RW Steinbrech, F Boroomand, E Wessel, F Meschke, A Zuev, O Teller, H Nickel, and L Singheiser. Defect formation and mechanical stability of perovskites based on LaCrO_3 for solid oxide fuel cells (SOFC). *Journal of the European Ceramic Society*, 23(16):3009–3020, 2003.
- Youngjae Hong, Pilgyu Byeon, Jumi Bak, Yoon Heo, Hye-Sung Kim, Hyung Bin Bae, and Sung-Yoon Chung. Local-electrostatics-induced oxygen octahedral distortion in perovskite oxides and insight into the structure of ruddlesden–popper phases. *Nature communications*, 12(1):1–10, 2021.
- Ryan Jacobs, Tam Mayeshiba, John Booske, and Dane Morgan. Material discovery and design principles for stable, high activity perovskite cathodes for solid oxide fuel cells. *Advanced Energy Materials*, 8(11):1702708, 2018.
- Anubhav Jain, Shyue Ping Ong, Geoffroy Hautier, Wei Chen, William Davidson Richards, Stephen Dacek, Shreyas Cholia, Dan Gunter, David Skinner, Gerbrand Ceder, et al. Commentary: The materials project: A materials genome approach to accelerating materials innovation. *APL materials*, 1(1):011002, 2013.
- Fanhao Jia, Shunbo Hu, Shaowen Xu, Heng Gao, Guodong Zhao, Paolo Barone, Alessandro Stroppa, and Wei Ren. Persistent spin-texture and ferroelectric polarization in 2d hybrid perovskite benzylammonium lead-halide. *The journal of physical chemistry letters*, 11(13):5177–5183, 2020.
- Jiahui Jia, Xu He, Arsalan Akhtar, Gervasi Herranz, and Miguel Pruneda. Dynamic control of octahedral rotation in perovskites by defect engineering. *Physical Review B*, 105(22):224112, 2022.
- C-Q Jin, J-S Zhou, JB Goodenough, QQ Liu, JG Zhao, LX Yang, Y Yu, RC Yu, T Katsura, A Shatskiy, et al. High-pressure synthesis of the cubic perovskite BaRuO_3 and evolution of ferromagnetism in ARuO_3 ($A = \text{Ca}, \text{Sr}, \text{Ba}$) ruthenates. *Proceedings of the National Academy of Sciences*, 105(20):7115–7119, 2008.
- Mats Johnsson and Peter Lemmens. *Crystallography and Chemistry of Perovskites*. John Wiley & Sons, Ltd, 2007. ISBN 9780470022184.
- Qiang Li, Kun Lin, Zhanning Liu, Lei Hu, Yili Cao, Jun Chen, and Xianran Xing. Chemical diversity for tailoring negative thermal expansion. *Chemical Reviews*, 122(9):8438–8486, 2022.
- Wei Li, Zheming Wang, Felix Deschler, Song Gao, Richard H Friend, and Anthony K Cheetham. Chemically diverse and multifunctional hybrid organic–inorganic perovskites. *Nature Reviews Materials*, 2(3):1–18, 2017.

- Wei Li, Ryan Jacobs, and Dane Morgan. Data and supplemental information for predicting the thermodynamic stability of perovskite oxides using machine learning models. *Data in brief*, 19: 261–263, 2018a.
- Wei Li, Ryan Jacobs, and Dane Morgan. Predicting the thermodynamic stability of perovskite oxides using machine learning models. *Computational Materials Science*, 150:454–463, 2018b.
- Xiuzhi Li, Zujian Wang, Chao He, Ying Liu, Xifa Long, Shujuan Han, and Shilie Pan. High piezoelectric response of a new ternary ferroelectric Pb (Ho_{1/2}Nb_{1/2}) O₃-Pb (Mg_{1/3}Nb_{2/3}) O₃-PbTiO₃ single crystal. *Materials Letters*, 143:88–90, 2015.
- Mingli Liang, Weihua Lin, Zhenyun Lan, Jie Meng, Qian Zhao, Xianshao Zou, Ivano E Castelli, Tonu Pullerits, Sophie E Canton, and Kaibo Zheng. Electronic structure and trap states of two-dimensional ruddlesden–popper perovskites with the relaxed goldschmidt tolerance factor. *ACS Applied Electronic Materials*, 2(5):1402–1412, 2020.
- Zhenhua Liang, Kaibin Tang, Qian Shao, Guocan Li, Suyuan Zeng, and Huagui Zheng. Synthesis, crystal structure, and photocatalytic activity of a new two-layer ruddlesden–popper phase, Li₂CaTa₂O₇. *Journal of Solid State Chemistry*, 181(4):964–970, 2008.
- Han Liu, John Lafferty, and Larry Wasserman. The nonparanormal: Semiparametric estimation of high dimensional undirected graphs. *Journal of Machine Learning Research*, 10(10), 2009.
- Miao Liu, Ziqin Rong, Rahul Malik, Pieremanuele Canepa, Anubhav Jain, Gerbrand Ceder, and Kristin A Persson. Spinel compounds as multivalent battery cathodes: a systematic evaluation based on ab initio calculations. *Energy & Environmental Science*, 8(3):964–974, 2015.
- David P MacKinnon. *Introduction to statistical mediation analysis*. Routledge, 2012.
- Warren S McCulloch and Walter Pitts. A logical calculus of the ideas immanent in nervous activity. *The bulletin of mathematical biophysics*, 5:115–133, 1943.
- Abanti Nag and V Shubha. Oxide thermoelectric materials: A structure–property relationship. *Journal of electronic materials*, 43:962–977, 2014.
- F. Pedregosa, G. Varoquaux, A. Gramfort, V. Michel, B. Thirion, O. Grisel, M. Blondel, P. Prettenhofer, R. Weiss, V. Dubourg, J. Vanderplas, A. Passos, D. Cournapeau, M. Brucher, M. Perrot, and E. Duchesnay. Scikit-learn: Machine learning in Python. *Journal of Machine Learning Research*, 12:2825–2830, 2011.
- Payam Refaeilzadeh, Lei Tang, Huan Liu, et al. Cross-validation. *Encyclopedia of database systems*, 5:532–538, 2009.
- Jörg Richter, Peter Holtappels, Thomas Graule, Tetsuro Nakamura, and Ludwig J Gauckler. Materials design for perovskite SOFC cathodes. *Monatshefte für Chemie-Chemical Monthly*, 140(9): 985–999, 2009.

- James E Saal, Scott Kirklin, Muratahan Aykol, Bryce Meredig, and Christopher Wolverton. Materials design and discovery with high-throughput density functional theory: the open quantum materials database (OQMD). *Jom*, 65:1501–1509, 2013.
- Florian H Schader, George A Rossetti Jr, Jun Luo, and Kyle G Webber. Piezoelectric and ferroelectric properties of $\text{Pb}(\text{In}_{1/2}\text{Nb}_{1/2})\text{O}_3$ - $\text{Pb}(\text{Mg}_{1/3}\text{Nb}_{2/3})\text{O}_3$ - PbTiO_3 single crystals under combined thermal and mechanical loading. *Acta Materialia*, 126:174–181, 2017.
- Kexin Song, Zhenrong Li, Haisheng Guo, Zhuo Xu, and Shiji Fan. Compositional segregation and electrical properties characterization of [001]-and [011]-oriented co-growth $\text{Pb}(\text{In}_{1/2}\text{Nb}_{1/2})\text{O}_3$ - $\text{Pb}(\text{Mg}_{1/3}\text{Nb}_{2/3})\text{O}_3$ - PbTiO_3 single crystal. *Journal of Applied Physics*, 123(15):154107, 2018.
- Mingzi Sun, Alan William Dougherty, Bolong Huang, Yuliang Li, and Chun-Hua Yan. Accelerating atomic catalyst discovery by theoretical calculations-machine learning strategy. *Advanced Energy Materials*, 10(12):1903949, 2020.
- Kenneth S Suslick. Encyclopedia of physical science and technology. *Sonoluminescence and sonochemistry, 3rd edn. Elsevier Science Ltd, Massachusetts*, pages 1–20, 2001.
- Vladimir Vapnik. Statistical learning theory. John Wiley & Sons, Inc., New York, 1, 1998.
- Vladimir Vapnik. *The nature of statistical learning theory*. Springer science & business media, 1999.
- Zujian Wang, Chao He, Xiuzhi Li, Ying Liu, Xifa Long, Shujuan Han, and Shilie Pan. Scandium modified lead magnesium niobate-lead titanate single crystals for high temperature and high power applications. *Materials Letters*, 184:162–165, 2016.
- Logan Ward, Ankit Agrawal, Alok Choudhary, and Christopher Wolverton. A general-purpose machine learning framework for predicting properties of inorganic materials. *npj Computational Materials*, 2(1):1–7, 2016.
- Robert B Wexler, Gopalakrishnan Sai Gautam, Ellen B Stechel, and Emily A Carter. Factors governing oxygen vacancy formation in oxide perovskites. *Journal of the American Chemical Society*, 143(33):13212–13227, 2021.
- Patrick M Woodward. Octahedral tilting in perovskites. i. geometrical considerations. *Acta Crystallographica Section B: Structural Science*, 53(1):32–43, 1997.
- Jingnan Xue and Faming Liang. A robust model-free feature screening method for ultrahigh-dimensional data. *Journal of Computational and Graphical Statistics*, 26(4):803–813, 2017.
- Ikuya Yamada, Kazuhide Takata, Naoaki Hayashi, Satoshi Shinohara, Masaki Azuma, Shigeo Mori, Shigetoshi Muranaka, Yuichi Shimakawa, and Mikio Takano. A perovskite containing quadrivalent iron as a charge-disproportionated ferrimagnet. *Angewandte Chemie*, 120(37):7140–7143, 2008.

Jianfa Zhao, Jiacheng Gao, Wenmin Li, Yuting Qian, Xudong Shen, Xiao Wang, Xi Shen, Zhiwei Hu, Cheng Dong, Qingzhen Huang, et al. A combinatory ferroelectric compound bridging simple ABO₃ and a-site-ordered quadruple perovskite. *Nature communications*, 12(1):1–9, 2021.

J-S Zhou. Structural distortions in rare-earth transition-metal oxide perovskites under high pressure. *Physical Review B*, 101(22):224104, 2020.